



RESEARCH ARTICLE | JUNE 02 2025

Gallium oxide/indium gallium zinc oxide heterojunction Schottky barrier thin-film transistors with ultrahigh 2D electron density over $6 \times 10^{13}/\text{cm}^2$ ✓

Jinxu Zhao ; Zhiyu Lin ; Chen Wang ; Xinghan Cai ; Jun Yu ; Lu Kang; Ying Wu; Jeffrey Xu; Mengwei Si



J. Vac. Sci. Technol. A 43, 043409 (2025)

<https://doi.org/10.1116/5.0268479>



Articles You May Be Interested In

High-performance IGZO/Ga₂O₃ dual-active-layer thin film transistor for deep UV detection

Appl. Phys. Lett. (June 2022)

High mobility crystallized stacked-channel thin-film transistors induced by low-temperature thermal annealing

Appl. Phys. Lett. (January 2025)

Enhancing photodetection performance of UV photodetectors with stacked Pt/NiO dual capping layers on IGZO thin-film transistors

AIP Advances (July 2023)

 **Advance your science and your career as a member of AVS**

[LEARN MORE](#)

Gallium oxide/indium gallium zinc oxide heterojunction Schottky barrier thin-film transistors with ultrahigh 2D electron density over $6 \times 10^{13}/\text{cm}^2$

Cite as: J. Vac. Sci. Technol. A 43, 043409 (2025); doi: 10.1116/5.0268479

Submitted: 14 April 2025 · Accepted: 15 May 2025 ·

Published Online: 2 June 2025



View Online



Export Citation



CrossMark

Jinxiu Zhao,¹  Zhiyu Lin,¹  Chen Wang,^{1,a)} Xinghan Cai,¹  Jun Yu,²  Lu Kang,³ Ying Wu,³ Jeffrey Xu,³ and Mengwei Si^{1,4,a)} 

AFFILIATIONS

¹School of Information Science and Electronic Engineering, Shanghai Jiao Tong University, Shanghai 200240, China

²School of Information Science and Engineering, Shandong University, Qingdao, Shandong 266000, China

³Huawei Technologies Company Ltd., Shenzhen 518129, China

⁴State Key Laboratory of Radio Frequency Heterogeneous Integration, Shanghai Jiao Tong University, Shanghai 200240, China

^{a)}Authors to whom correspondence should be addressed: wangchen96@sjtu.edu.cn and mengwei.si@sjtu.edu.cn

ABSTRACT

To enhance the current driving capability of oxide semiconductor thin-film transistors (TFTs) is a key challenge in emerging display applications that request high resolution and brightness, such as micro-light-emitting diode. In general, increasing the indium content in indium gallium zinc oxide (IGZO) to achieve high mobility is the most common method, but indium-rich IGZO TFTs suffer from negative threshold voltage (V_{TH}) and poor stability. In this work, a novel high on-current enhancement-mode Schottky barrier TFT is fabricated through the $\text{Ga}_2\text{O}_3/\text{IGZO}$ heterojunction and Ni/IGZO Schottky junction. A high-density two-dimensional electron gas with sheet carrier density over $6 \times 10^{13}/\text{cm}^2$ is achieved, by introducing an oxygen-vacancy-rich $\text{Ga}_2\text{O}_3/\text{IGZO}$ interface. The sheet carrier density is beyond the gate control limitation, leading to a low channel resistance. The source/drain Schottky junction is achieved through defect engineering by Ga_2O_3 growth and etching at the Ni/IGZO interface. The Schottky barrier can be modulated by gate voltage so that the device can be turned off with a large V_{TH} of ~ 1 V. The proposed $\text{Ga}_2\text{O}_3/\text{IGZO}$ Schottky barrier heterojunction TFT enables a new approach to enhance the current driving capability of oxide TFTs beyond conventional material engineering for high mobility.

Published under an exclusive license by the AVS. <https://doi.org/10.1116/5.0268479>

I. INTRODUCTION

Since the discovery of oxide semiconductors, such as amorphous indium gallium zinc oxide (IGZO), oxide semiconductor thin-film transistors (TFTs) have been extensively used in flat panel displays because of their excellent performance, such as low leakage, much higher mobility than amorphous Si, large-area uniformity, and low cost.^{1–5} However, the driving current of IGZO TFTs is still not enough with a mobility of about $10\text{--}30\text{ cm}^2/\text{V s}$.^{6,7} Thus, low-temperature polycrystalline silicon (LTPS) TFTs with much higher mobility (about $100\text{ cm}^2/\text{V s}$)⁸ are frequently employed together with IGZO TFTs as low-temperature polycrystalline oxide (LTPO) technology to enhance the current driving

capability.^{9–11} However, the high production costs, high process temperature, large leakage current, and difficulty with the process in large-areas have limited the employment of LTPS in large-area display applications. To achieve high-mobility oxide semiconductors, TFTs would significantly benefit display technology.

Some approaches have been adopted to develop high-mobility oxide semiconductors, such as indium-rich compound,^{12–14} new elements' introduction,^{15–17} metal-induced crystallization,^{18–20} and design of sequential layer deposition.^{21–23} Although there have been many works reporting rather high-mobility oxide TFTs, these methods often suffer from nonideal effects, such as bad stability, negative shift of threshold voltage (V_{TH}), and deterioration of

20 June 2025 07:54:28

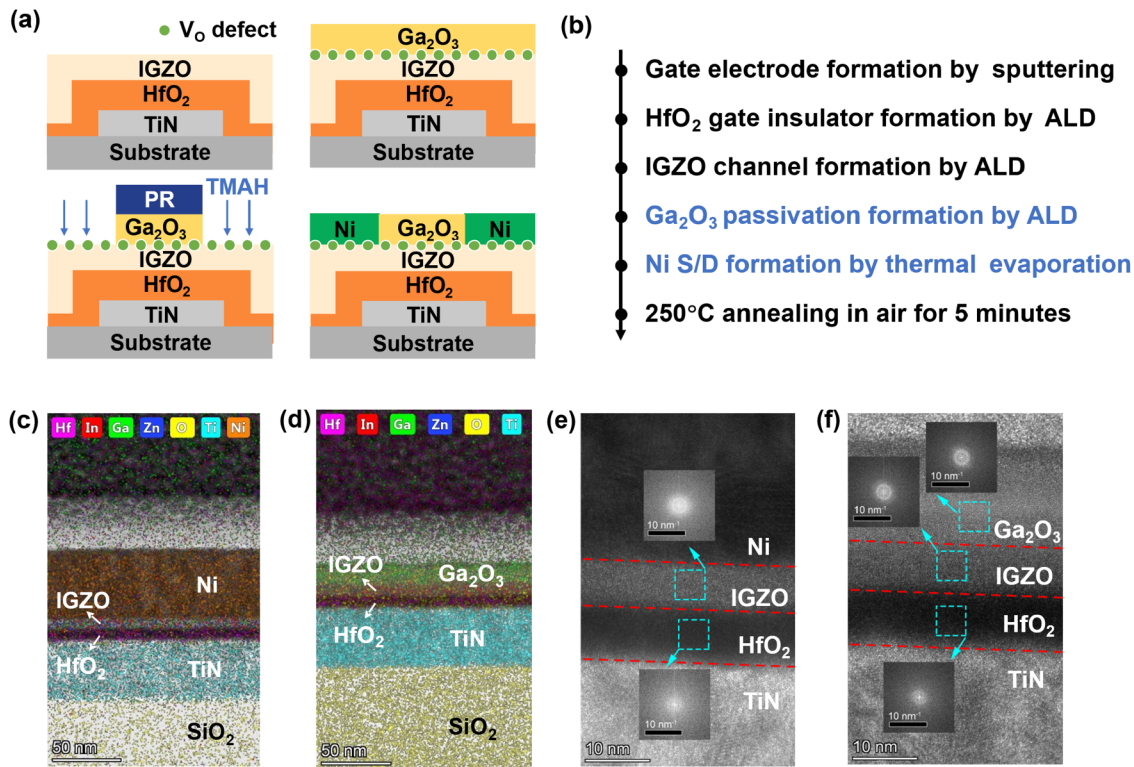


FIG. 1. (a) Schematic and (b) device fabrication process flow of a Ga₂O₃/IGZO heterojunction transistor, highlighting the key process steps. The cross-sectional STEM and EDS images of a Ga₂O₃/IGZO heterojunction transistor at (c) S/D region and (d) channel region. HRTEM images of a Ga₂O₃/IGZO heterojunction transistor at (e) S/D region and (f) channel region, with corresponding FFT images at different locations.

20 June 2025 07:54:29

subthreshold swing (SS). As a result, the mobility-stability trade-off becomes a well-known issue for high-mobility oxide semiconductor TFTs.¹⁶ Thus, enhancing the driving current of oxide semiconductor TFT by mobility engineering without sacrificing stability and reliability is very challenging.

Here, the Schottky barrier TFT can offer another path to overcome the above issues, where the on/off switching is determined by controlling the source/drain (S/D) Schottky barrier height (Φ_B).^{24–29} Meanwhile, the current driving capability can be significantly enhanced with a high-carrier-density channel. However, an oxide semiconductor with high carrier density is necessary to achieve a highly conductive channel, but a high carrier density would result in low effective Φ_B , resulting in a poor on/off ratio. Therefore, to form a gate-controllable Schottky barrier at S/D contact and a highly conductive channel on the same device are the key to realize the Schottky barrier oxide TFT with high drive current.

In this work, a highly conductive Ga₂O₃/IGZO heterojunction channel was grown by the atomic layer deposition (ALD) of the Ga₂O₃/IGZO bilayer. High-density oxygen vacancies (V_O) are formed near the Ga₂O₃/IGZO interface due to the broken In–O bond, which was identified by the x-ray photoelectron spectroscopy (XPS) depth profile, leading to a high-density two-dimensional

electron gas (2DEG) over $6 \times 10^{13}/\text{cm}^2$ beyond the gate control limitation. The S/D contact was fabricated by the selective etching of Ga₂O₃ over IGZO and followed by the deposition of Ni as the S/D contact was deposited as S/D contact. A gate-controllable Schottky junction is formed due to the V_O -rich Ni/IGZO contact without introducing high carrier density in the semiconductor. As a result, an enhancement-mode Schottky barrier TFT is achieved with higher drain current than conventional TFT with the same IGZO channel and Ni contact.

II. EXPERIMENT

The Ga₂O₃/IGZO heterojunction TFTs with a bottom-gate and top-contact structure were used in this work. The devices were fabricated on an Si wafer with 90 nm thermally grown SiO₂. TiN was used as the gate electrode. A 7 nm HfO₂ gate insulator and a 7 nm IGZO channel were deposited by ALD. Three types of devices were designed: Ga₂O₃-first (Ga₂O₃ deposited before S/D contact formation) [Figs. 1(a) and 1(b)], Ga₂O₃-last (Ga₂O₃ deposited after S/D contact formation), and without Ga₂O₃ (both shown in Fig. S1 in the supplementary material), for investigating the Schottky junction formation mechanism and the properties of the channel. The Ga₂O₃-first devices are the Ga₂O₃/IGZO

heterojunction Schottky barrier TFT proposed in this work, while the Ga₂O₃-last and without Ga₂O₃ devices are the control group. For the Ga₂O₃-first devices, after patterning of IGZO, the Ga₂O₃ layers were deposited using ALD. The patterning of Ga₂O₃ was achieved simultaneously with S/D lithography, where the 2.38% tetramethylammonium hydroxide (TMAH) developer could etch Ga₂O₃ under the S/D contact, but IGZO was retained. 40 nm Ni S/D electrodes were formed by thermal evaporation and lift-off method. For the Ga₂O₃-last devices, the Ga₂O₃ layers were grown after the S/D formation of 40 nm Ni. For the devices without Ga₂O₃, no Ga₂O₃ layer was deposited after IGZO patterning and S/D deposition. Finally, the Ga₂O₃-first devices and the Ga₂O₃-last devices were annealed in air at 250 °C for 5 min.

The roughness of the IGZO thin films with and without Ga₂O₃ was characterized by atomic force microscope (AFM) (Cypher S, Asylum Research). Transmission electron microscopy (TEM) (TALOS F200X, Thermo Fisher) was conducted to analyze the Ga₂O₃/IGZO heterojunction Schottky barrier TFT at the S/D region and channel region. Secondary ion mass spectrometry (SIMS) (ToF-SIMS 5-100, ION-TOF GmbH) analyses were used to find the concentration variations in Hf, In, Ga, Zn, O, and H elements in the depth profile of IGZO thin films. Chemical bond states at the Ga₂O₃/IGZO heterojunction and S/D contact region were analyzed by x-ray photoelectron spectroscopy (XPS) (AXIS Ultra DLD, Kratos) with a depth profile by Ar⁺ etching, which was carried out using a monochromatic Al K α (1486.6 eV) source.

The electrical properties of the devices were measured using a B1500A semiconductor parameter analyzer. The gated Hall bar devices were fabricated together with TFTs to evaluate the Hall mobility (μ_H) and sheet carrier density (n_{2D}) of the 2DEG at the channel region. The Hall measurement was performed based on the ASTM F76 standard with a Hall bar structure to avoid the distortion of geometry in the regularly used van der Pauw samples (see Sec. V in the [supplementary material](#) for details). The voltage parallel to I_D and Hall voltage were measured by a SR830 lock-in amplifier, and the gate voltage was applied by Keithley 2400. The gated Hall measurement was carried out in a physical property measurement system (PPMS) (DynaCool-14T). The driven AC signal has a frequency of 499 Hz and an amplitude of 0.1 V_{RMS}.

III. RESULTS AND DISCUSSION

A. Characterization of Ni/IGZO and Ga₂O₃/IGZO interfaces

The scanning transmission electron microscopy (STEM) and energy dispersive spectroscopy (EDS) images of a fabricated Ga₂O₃/IGZO heterojunction Schottky barrier TFT at the S/D region [Fig. 1(c)], and the STEM and energy dispersive channel region [Fig. 1(d)]. Figures 1(e) and 1(f) illustrate the corresponding high-resolution transmission electron microscopy (HRTEM) and fast Fourier transform (FFT) images, where both Ga₂O₃ and IGZO are amorphous. It is clear that Ga₂O₃ on top of IGZO at the S/D region was completely etched. AFM topological images of the as-deposited IGZO thin film, IGZO covered with Ga₂O₃, and IGZO covered with Ga₂O₃ after the wet etching of Ga₂O₃ are shown in Fig. S2 in the [supplementary material](#). The root-mean-square (RMS) roughness values are estimated to be 0.157 ~ 0.214 nm, showing

smooth morphologies and slight damage to the IGZO surface after wet etching. In addition, ToF-SIMS was used to characterize the depth distribution of elements at the S/D contact region [Fig. S3(a) in the [supplementary material](#)] and channel region [Fig. S3(b) in the [supplementary material](#)]. The oxygen concentration of IGZO in the two regions remains relatively stable. The concentration of indium and zinc at the Ga₂O₃/IGZO and Ni/IGZO interface shows a sharp change, reflecting almost no In or Zn diffusion. The H peak is observed at the Ga₂O₃/IGZO and Ni/IGZO interfaces, indicating that there may exist hydrogen-related defects at the interfaces.

In order to further explore the interface defects, Fig. 2(a) shows the XPS depth profile by Ar⁺ etching at the S/D contact region. The Ni 2p_{3/2} spectra contain a strong peak at 852.3 eV representing Ni⁰ and a weak peak at 853.5 eV corresponding to oxidized Ni²⁺. There are two strong peaks in In 3d_{5/2} spectra located at 445.1 and 443.3 eV, representing In³⁺ and In⁰, respectively. The In³⁺ peak represents the In³⁺ bonds to the O²⁻ (In–O). Due to the poor stability of the In–O bond, there are more oxygen vacancies around the indium atom, resulting in the appearance of the metal indium (In⁰).^{30,31} Therefore, the intensity of the In⁰ peak serves as a direct measure of this charge compensation, indirectly indicating the concentration of oxygen vacancies. The intensity of the In⁰ peak decreases with the Ar⁺ etching time, suggesting the existence of a high density of V_O near the Ni/IGZO interface due to the broken In–O bond. The Ga 2p_{3/2} and Zn 2p_{3/2} spectra remain similar at different depths, indicating that Ga–O and Zn–O bonds are more stable. A subpeak related to O-related defects occurs in O 1s spectra, which may be caused by oxygen vacancies, hydroxyl (–OH) or weakly bonded oxygen. The defects at Ni/IGZO interface are likely caused by Ga₂O₃ growth and etching. Figure 2(b) shows the XPS depth profile at the channel region. The behaviors of In 3d_{5/2}, Ga 2p_{3/2}, Zn 2p_{3/2}, and O 1s are similar to that at the S/D region, suggesting that a high density of V_O also occurs near the Ga₂O₃/IGZO interface.

B. Impact of Ga₂O₃ passivation on the I–V characteristics

To investigate the impact of V_O on the channel region and the S/D region of Ga₂O₃/IGZO TFT, devices with three types of Ga₂O₃ passivation stack were fabricated. Figures 3(a)–3(c) present the transfer curves and field-effect mobility (μ_{FE}) extracted at low V_{DS} for IGZO TFTs with a channel length (L_{ch}) of 10 μ m. Both the without Ga₂O₃ and Ga₂O₃-last devices are ohmic contacts; a significant difference between the without Ga₂O₃ device V_{TH} = 0.6 V and the Ga₂O₃-last device V_{TH} = –1.9 V is additional evidence that the growth of Ga₂O₃ increases the carrier concentration. The comparison of I_D at a V_{DS} of 1.2 V and μ_{FE} is shown in Figs. 3(d) and 3(e). As can be seen, the Ga₂O₃-last device has a larger I_D than the device without Ga₂O₃, which proves that Ga₂O₃/IGZO heterojunction enhanced I_D significantly compared to IGZO only. The Ga₂O₃-first device can achieve the same driving current at a lower voltage, significantly reducing power consumption. However, the Ga₂O₃-last device cannot be turned off and the μ_{FE} of the Ga₂O₃-last device is similar to the device without Ga₂O₃. Based on the XPS results, it can be inferred that a highly conductive Ga₂O₃/IGZO channel is formed in the Ga₂O₃-last device due to the

20 June 2025 07:54:29

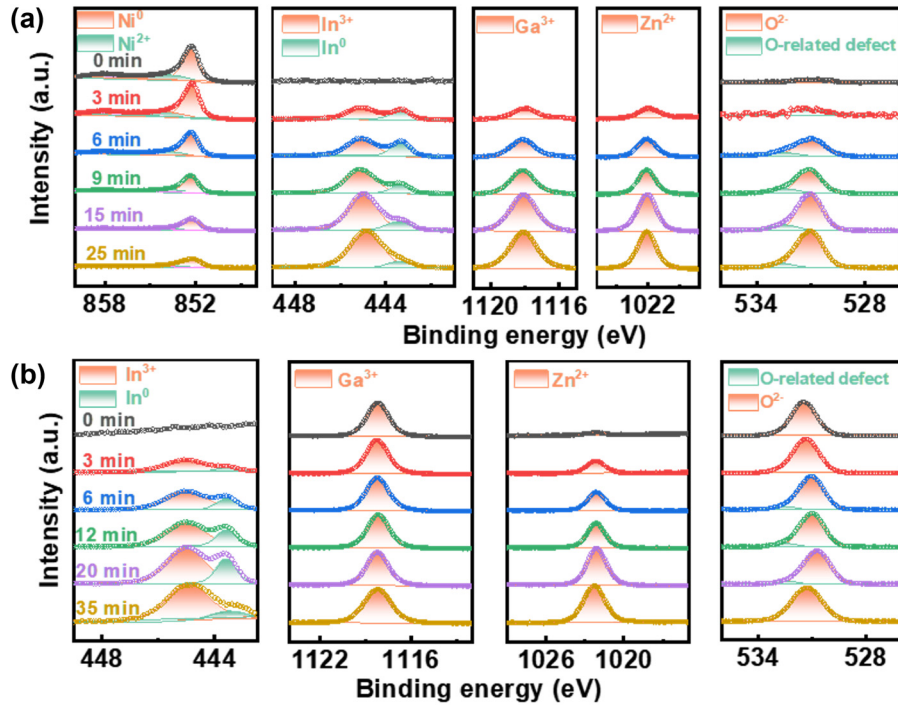


FIG. 2. XPS depth profile of a Ga₂O₃/IGZO heterojunction transistor at (a) channel and (b) S/D contact region.

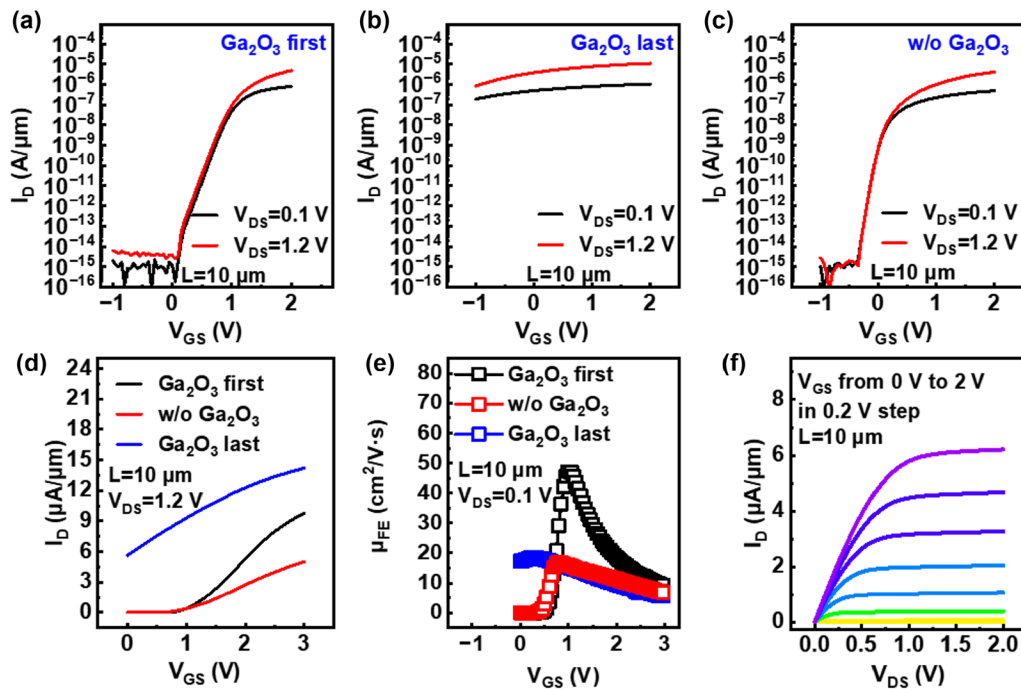


FIG. 3. Comparison of transfer curves of different passivation (a) Ga₂O₃ first, (b) Ga₂O₃ last, and (c) without Ga₂O₃. (d) I_D - V_{GS} characteristics in linear scale and (e) μ_{FE} - V_{GS} of IGZO TFTs with different passivation. (f) Output curves of a Ga₂O₃/IGZO heterojunction transistor.

20 June 2025 07:54:29

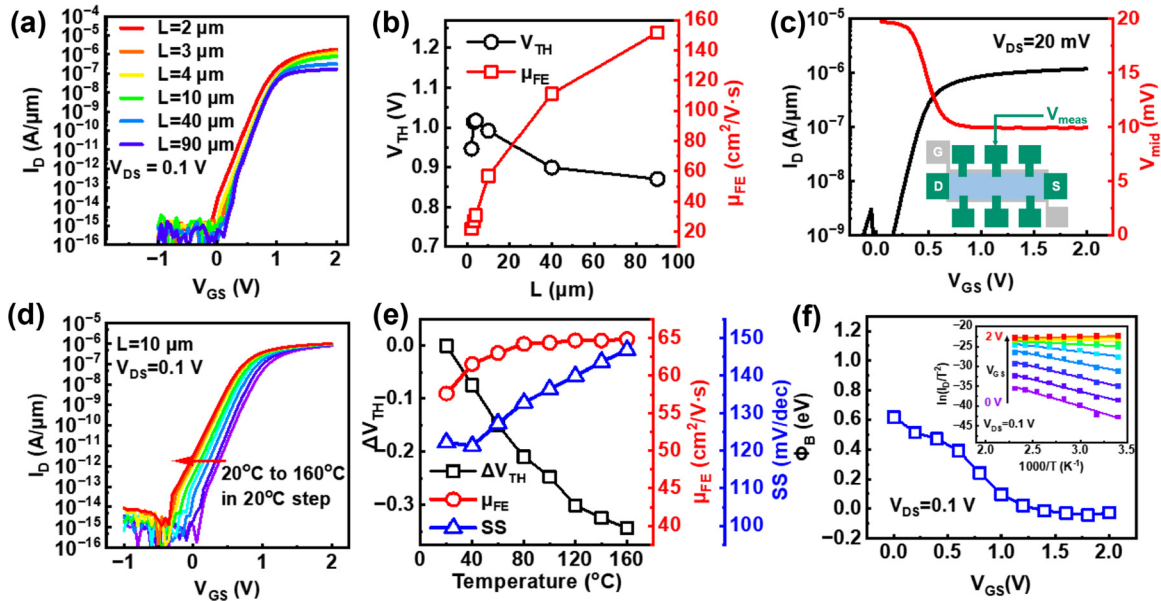


FIG. 4. (a) L-dependent transfer curve of Ga₂O₃/IGZO heterojunction transistors. (b) L-dependent V_{TH} and μ_{FE} . (c) $I_D - V_{GS}$ and $V_{mid} - V_{GS}$ characteristics measured in a gated Hall bar structure of the Ga₂O₃/IGZO heterojunction transistor. (d) Temperature-dependent transfer curves of a Ga₂O₃/IGZO heterojunction transistor with $L = 10 \mu\text{m}$. (e) Temperature-dependent V_{TH} , μ_{FE} , and SS of the Ga₂O₃/IGZO heterojunction transistor. (f) Contact Schottky barrier height at various V_{GS} extracted from Arrhenius plot with linear fitting at different V_{GS} .

high density of V_O at the Ga₂O₃/IGZO interface so that a high-density 2DEG is generated exceeding the limit of gate control. The large I_D of the Ga₂O₃-last device also demonstrates that ohmic Ni/IGZO contacts can be formed without any treatment. For the Ga₂O₃-first device with $L_{ch} = 10 \mu\text{m}$, a high maximum μ_{FE} of $57.6 \text{ cm}^2/(\text{V s})$, a positive V_{TH} of 1 V, and an SS of 122.15 mV/dec are simultaneously achieved in Fig. 3(a). The highly conductive Ga₂O₃/IGZO channel contributes to the high apparent μ_{FE} , and the off-state is more likely to be contributed by the Schottky barrier at the S/D region. In addition, Fig. 3(f) shows the $I_D - V_{DS}$ characteristics of the Ga₂O₃-first device with $L_{ch} = 10 \mu\text{m}$, including linear and saturation regions. The Ga₂O₃-first device has no exponential $I_D - V_{DS}$ relation at low V_{DS} shown in Fig. 3(f), which may be due to the combined effects of barrier inhomogeneity and thin semiconductor thickness.³²

To further examine the operation mechanism in Ga₂O₃/IGZO heterostructure TFTs, a series of electrical characterizations were performed. The devices with different channel lengths were fabricated, and the L_{ch} -dependent transfer curves are plotted in Fig. 4(a). Figure 4(b) summarizes the V_{TH} and μ_{FE} scaling metrics extracted from transfer curves. With increasing L_{ch} , V_{TH} changes slightly and μ_{FE} increases significantly to $151.66 \text{ cm}^2/\text{V s}$ at $L_{ch} = 90 \mu\text{m}$. The scaling metrics of μ_{FE} in the Ga₂O₃-first device are different from traditional TFTs with ohmic contact, which means that the modulation of I_D in Ga₂O₃/IGZO heterojunction Schottky barrier TFTs is mainly attributed to the gate control of the Ni/IGZO Schottky junction at the S/D region. Note that the heterojunction structure may not be suitable for

short channel devices, as μ_{FE} decreases with L_{ch} scaling (see Sec. IV in the supplementary material for details), but it will play a significant role for driving TFTs in display applications at an L_{ch} of a few μm .³³

C. Measurements of Schottky barrier and channel 2DEG

To reveal the working mechanism, a gated Hall bar device is fabricated to capture the voltage drop across the S/D contact

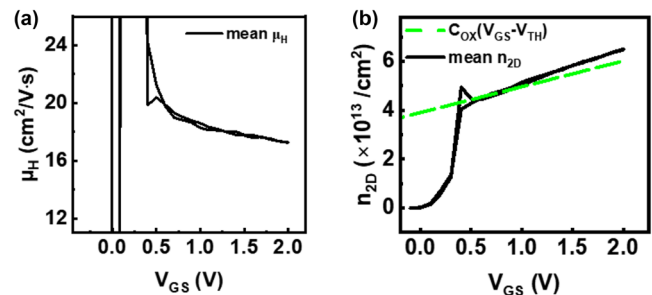


FIG. 5. Extracted mean (a) μ_H and (b) n_{2D} of a gated Hall bar with Ga₂O₃/IGZO heterojunction under $\pm 1, \pm 3, \pm 5 \text{ T}$ at different V_{GS} . The high n_{2D} is beyond the capability of gate control.

20 June 2025 07:54:29

TABLE I. Benchmarking of the relevant metal oxide TFT devices, including carrier density (n), L_{ch} , mobility (μ), V_{TH} , SS, and $I_{\text{ON}}/I_{\text{OFF}}$

Reference	n (cm^{-3})	L_{ch} (μm)	μ ($\text{cm}^2/\text{V s}$)	V_{TH} (V)	SS (V/dec)	$I_{\text{ON}}/I_{\text{OFF}}$
24	1.0×10^{17}	—	—	−1.6	0.2	1.0×10^8
25	1.2×10^{19}	100	20.4 ^a	5.8	0.4	2.0×10^7
26	1.8×10^{19}	12	16.1 ^b	−1.2	0.4	1.3×10^8
27	1.0×10^{18}	60	15.8 ^c	16.1	0.6	1.2×10^7
29	1.5×10^{18}	800	102.6 ^a	−6	1.1	1.0×10^6
This work	8.6×10^{19}	10	57.6 ^a	0.7	0.1	1.0×10^{9d}
		90	151.7 ^a			

^aThe apparent field-effect mobility extracted from the Schottky TFT.

^bThe apparent saturation mobility extracted from the Schottky TFT.

^cThe field effect mobility extracted from the ohmic contact TFT.

^dThe $I_{\text{ON}}/I_{\text{OFF}}$ ratio $\sim 1.0 \times 10^9$ for $V_{\text{GS}} = 2$ V and $V_{\text{DS}} = 1.2$ V, where I_{OFF} is limited by measurement detection limit.

[illustrated in Fig. 4(c)]. V_{DS} is fixed at 0.02 V, while V_{GS} sweeps from 0 to 2 V. In the V_{GS} range from 0 to 0.7 V at the subthreshold region, the mid-point voltage (V_{mid}) is higher than half of V_{DS} . It can be deduced that the voltage drop is mainly on the source contact, because the Schottky junction at the source contact is reversely biased and the potential barrier is high at the subthreshold region. When V_{GS} further increases over 0.7 V, V_{mid} approaches half V_{DS} , indicating that the voltage drop is mainly across the channel region. Therefore, Φ_{B} can be lowered by the positive V_{GS} . Moreover, the contact resistance (R_{C}) is extracted from the transfer curves in Fig. 3(a) and plotted in Fig. S4 in the supplementary material, which decreases with the positive V_{GS} . The above results confirm the off-state of Ga_2O_3 -first devices is realized by a high Schottky barrier at source contact when V_{GS} is below V_{TH} . In addition, to further characterize the gate control of Φ_{B} , the $I_{\text{D}} - V_{\text{GS}}$ curves are measured under a V_{DS} of 0.1 V and V_{GS} from −1 to 2 V at the temperature range of 20 °C ~ 160 °C, as shown in Fig. 4(d). The $I_{\text{D}} - V_{\text{GS}}$ curves shift negatively at elevated temperature due to the enhanced thermal emission of electrons. Figure 4(e) summarizes the V_{TH} , μ_{FE} , and SS versus temperature characteristics. μ_{FE} does not change at high temperatures, suggesting a good thermal stability of the Schottky junction. Based on the thermal emission model, the I_{D} is determined by

$$I_{\text{D}} = A^* T^2 \exp\left(\frac{-\Phi_{\text{B}}}{k_{\text{B}} T}\right), \quad (1)$$

where A^* is the Richardson constant, T is the temperature, and k_{B} is the Boltzmann constant. The inset in Fig. 4(f) shows the $\ln(I_{\text{D}}/T)$ vs $1000/T$ characteristics, the slopes of which correspond to Φ_{B} , as shown in Fig. 4(f).³⁴ It is understood the fermi level (E_{F}) is pinned due to defects at the Ni/IGZO interface, so Φ_{B} is determined by the charge neutral level (CNL).³⁵

According to the above results, when the Schottky junction is formed with zero gate voltage, the E_{F} of IGZO and Ni are equal, and a Schottky barrier exists. If a positive gate voltage is applied, the IGZO depletion region width is narrower, leading to a low R_{C} , so that the device is in on-state. Meanwhile, a highly conductive $\text{Ga}_2\text{O}_3/\text{IGZO}$ channel promotes carrier transport from the source to drain. Both of two factors contribute to the high apparent

mobility and large output current at the long channel. On the contrary, under a negative gate voltage, the depletion region of IGZO becomes wider, making it more difficult for electron injection into the IGZO layer, so the device is in off-state.

The gated Hall measurement is performed at 300 K to evaluate μ_{H} and $n_{2\text{D}}$ at different V_{GS} . Figure 5(a) shows the extracted mean μ_{H} under ± 1 , ± 3 , ± 5 T to be ~ 17 $\text{cm}^2/\text{V s}$ at high V_{GS} , which is consistent with the μ_{FE} of the unpassivated IGZO thin film in Fig. 3(e). The extracted mean $n_{2\text{D}}$ is shown in Fig. 5(b), increasing linearly at high V_{GS} when the Schottky barrier is low, exhibiting a maximum $n_{2\text{D}}$ of $6.64 \times 10^{13}/\text{cm}^2$ (other details shown in Fig. S5 in the supplementary material). The maximum carrier density that can be controlled by V_{GS} is calculated as $C_{\text{ox}}(V_{\text{GS}} - V_{\text{TH}})$. Thus, as can be seen from the trend line in Fig. 5(b), the device cannot be turned off by the gate voltage only, verifying that the device turns off due to the modulation of Φ_{B} by V_{GS} .

Table I lists the relevant performance parameters of TFTs. It is evident that the $\text{Ga}_2\text{O}_3/\text{IGZO}$ heterojunction transistors exhibit ultrahigh current density, steep SS, and high $I_{\text{ON}}/I_{\text{OFF}}$ ratio.

IV. CONCLUSIONS

In conclusion, we demonstrate a Schottky barrier TFT with high-density 2DEG by introducing $\text{Ga}_2\text{O}_3/\text{IGZO}$ heterojunction and reveal its potential to enhance the driving current of oxide semiconductor TFTs. Through a detailed investigation of device operation, the role of V_{O} defects on the formation of high-density 2DEG at the channel region and Schottky barrier at the S/D region is clarified. Our findings provide a new route to improve current driving capability without improving channel mobility.

SUPPLEMENTARY MATERIAL

See the supplementary material for the additional details on device fabrication, AFM, ToF-SIMS, R_{C} , and Hall characterization.

ACKNOWLEDGMENTS

The authors acknowledge the funding support through STI 2030-Major Projects (Grant No. 2022ZD0210600), Shanghai Pilot Program for Basic Research—Shanghai Jiao Tong University

20 June 2025 07:54:29

(Grant Nos. 21TQ1400212 and 21TQ1400206), and National Natural Science Foundation of China (Grant Nos. 62274107 and 92264204).

AUTHOR DECLARATIONS

Conflict of Interest

The authors have no conflicts to disclose.

Author Contributions

J.Z. and Z.L. contributed equally to this work.

Jinxu Zhao: Data curation (equal); Formal analysis (equal); Investigation (equal); Writing – original draft (equal). **Zhiyu Lin:** Data curation (equal); Formal analysis (equal); Investigation (equal); Writing – review & editing (equal). **Chen Wang:** Data curation (equal); Formal analysis (equal); Investigation (equal); Writing – original draft (equal). **Xinghan Cai:** Resources (equal); Writing – review & editing (equal). **Jun Yu:** Investigation (equal); Writing – review & editing (equal). **Lu Kang:** Investigation (equal); Writing – review & editing (equal). **Ying Wu:** Investigation (equal); Supervision (equal); Writing – review & editing (equal). **Jeffrey Xu:** Supervision (equal); Writing – review & editing (equal). **Mengwei Si:** Conceptualization (equal); Formal analysis (equal); Investigation (equal); Supervision (equal); Writing – review & editing (equal).

DATA AVAILABILITY

The data that support the findings of this study are available from the corresponding authors upon reasonable request.

REFERENCES

- ¹K. Nomura, H. Ohta, A. Takagi, T. Kamiya, M. Hirano, and H. Hosono, *Nature* **432**, 488 (2004).
- ²H. H. Hsieh, H. H. Lu, H. C. Ting, C. S. Chuang, C. Y. Chen, and Y. Lin, *J. Inf. Disp.* **11**, 160 (2010).
- ³S. Li, M. Tian, Q. Gao, M. Wang, T. Li, Q. Hu, X. Li, and Y. Wu, *Nat. Mater.* **18**, 1091 (2019).
- ⁴Z. Lin, Z. Wang, J. Zhao, X. Li, and M. Si, *IEEE Electron Device Lett.* **44**, 536 (2023).
- ⁵D. Geng, K. Wang, L. Li, K. Myny, A. Nathan, J. Jang, Y. Kuo, and M. Liu, *Nat. Electron.* **6**, 963 (2023).
- ⁶J. H. Lee *et al.*, *SID Symposium Digest Technical Papers* (Wiley, New York, 2008), Vol. 39, p. 625.

- ⁷Y. Hara, T. Kikuchi, H. Kitagawa, J. Morinaga, H. Ohgami, H. Imai, T. Daitoh, and T. Matsuo, *J. Soc. Inf. Disp.* **26**, 169 (2018).
- ⁸M. Mativenga, D. Geng, and J. Jang, *SID Symposium Digest Technical Papers* (Wiley, New York, 2014), Vol. 45, p. 1.
- ⁹T.-K. Chang, C.-W. Lin, and S. Chang, *SID Symposium Digest Technical Papers* (Wiley, New York, 2019), Vol. 50, p. 545.
- ¹⁰W. Tang *et al.*, *IEEE International Electron Devices Meeting (IEDM)*, San Francisco, CA (IEEE, New York, 2022), p. 20.4.1.
- ¹¹Z. Wang *et al.*, *IEEE Trans. Electron Devices* **71**, 4664 (2024).
- ¹²M. Si *et al.*, *Nano Lett.* **21**, 500 (2021).
- ¹³M. Si, Z. Lin, Z. Chen, X. Sun, H. Wang, and P. D. Ye, *Nat. Electron.* **5**, 164 (2022).
- ¹⁴K. Hikake *et al.*, *2023 IEEE Symposium on VLSI Technology and Circuits (VLSI Technology and Circuits)*, Kyoto (IEEE, New York, 2023), p. T14-1.
- ¹⁵H. W. Zan, C. C. Yeh, H. F. Meng, C. C. Tsai, and L. H. Chen, *Adv. Mater.* **24**, 3509 (2012).
- ¹⁶Y.-S. Shiah, K. Sim, Y. Shi, K. Abe, S. Ueda, M. Sasase, J. Kim, and H. Hosono, *Nat. Electron.* **4**, 800 (2021).
- ¹⁷D.-G. Kim *et al.*, *ACS Appl. Mater. Interfaces* **15**, 31652 (2023).
- ¹⁸A. Y. Hwang, S. T. Kim, H. Ji, Y. Shin, and J. K. Jeong, *Appl. Phys. Lett.* **108**, 152111 (2016).
- ¹⁹Y. Shin, S. T. Kim, K. Kim, M. Y. Kim, S. Oh, and J. K. Jeong, *Sci. Rep.* **7**, 10885 (2017).
- ²⁰G. B. Kim, N. On, T. Kim, C. H. Choi, J. S. Hur, J. H. Lim, and J. K. Jeong, *Small Methods* **7**, 2201522 (2023).
- ²¹S. Lee, Y.-H. Kang, M.-S. Kim, H. Lee, Y.-H. Cho, M. Kim, T.-S. Yoon, H.-M. Kim, and K.-B. Kim, *ACS Appl. Mater. Interfaces* **12**, 39372 (2020).
- ²²S.-H. Moon, S.-H. Bae, Y.-H. Kwon, N.-J. Seong, K.-J. Choi, and S.-M. Yoon, *Ceram. Int.* **48**, 20905 (2022).
- ²³H. J. Seul, M. J. Kim, H. J. Yang, M. H. Cho, M. H. Cho, W.-B. Song, and J. K. Jeong, *ACS Appl. Mater. Interfaces* **12**, 33887 (2020).
- ²⁴S. H. Rha *et al.*, *IEEE Trans. Electron Devices* **60**, 1128 (2013).
- ²⁵T. T. Trinh, K. Jang, V. A. Dao, and J. Yi, *J. Appl. Phys.* **116**, 214504 (2014).
- ²⁶T. T. Trinh, K. Jang, S. Velumani, V. A. Dao, and J. Yi, *Mater. Sci. Semicond. Process.* **38**, 50 (2015).
- ²⁷X. Ji, Y. Yuan, X. Yin, S. Yan, Q. Xin, and A. Song, *IEEE Trans. Electron Devices* **69**, 6783 (2022).
- ²⁸C. Chen *et al.*, *Adv. Sci.* **6**, 1801189 (2019).
- ²⁹C. Wang, C. Zeng, W. Lu, H. Ning, F. Li, and F. Ma, *IEEE Electron Device Lett.* **44**, 646 (2023).
- ³⁰M. Mirzaee and A. Dolati, *J. Sol-Gel Sci. Technol.* **75**, 582 (2015).
- ³¹I. N. Reddy, C. Venkata Reddy, M. Cho, J. Shim, and D. Kim, *Mater. Res. Express* **4**, 086406 (2017).
- ³²J. Zhang, J. Wilson, G. Auton, Y. Wang, M. Xu, Q. Xin, and A. Song, *Proc. Natl. Acad. Sci. U.S.A.* **116**, 4843 (2019).
- ³³D. S. Schulman, A. J. Arnold, and S. Das, *Chem. Soc. Rev.* **47**, 3037 (2018).
- ³⁴S. Chand and J. Kumar, *J. Appl. Phys.* **82**, 5005 (1997).
- ³⁵S. Sze, Y. Li, and K. Ng, *Physics of Semiconductor Devices* (Wiley, New York, 2007), Chap. 3.

20 June 2025 07:54:29